Development of a high accurate numerical platform for the thermal and optical optimization of linear Fresnel receivers

Erick Guadamud[1], Jorge Chiva[1], Guillem Colomer[1], Joan Farnós[1], Ahmed Al Mers[2], Joaquim Rigola[1] and Carlos David Perez-Segarra[1]

[1] Heat and Mass Transfer Technological Center (CTTC), Terrassa (Spain)
Universitat Politècnica de Catalunya-BarcelonaTech (UPC), Terrassa (Spain)
ESEIAAT, Colom 11, E-08222 Terrassa, Barcelona, Spain
[2] Department of Energy, Ecole Nationale Superieure d'Arts et Metiers, Meknés, Morocco.

Abstract

This paper represents an advanced methodology for the detailed modeling of the heat transfer and fluids dynamics phenomena in Linear Fresnel receivers. The present work aims at modeling Linear Fresnel elements (e.g. insulation material, glass cover, tube, pipe, etc.) by proposing a parallel modular object-oriented methodology. The heat conduction, natural convection, single & two-phase flow, and solar & thermal radiation are solved and coupled in an adequate manner. The Navier-Stokes 3D equations with incompressible and turbulent fluid hypotheses are used to solve the fluid inside the cavity by means of a CFD&HT coupling with thermal and solar radiation. The heat flux incident on the tube is analyzed by a 3D conduction model to determine the temperature distribution, single or multiphase models can be used for the HTF. A Monte Carlo Ray-tracing method is applied to obtain the estimated solar radiation source as a function of the altitude and azimuth solar angles. This work presents a comparison of three configurations, their optical behavior, the effects of the receiver height, the orientation of the mirrors and the shadows, temperature, velocity and thermal flow profiles are analyzed and presented hereafter.

Keywords: Linear Fresnel Receivers, CFD&HT, Numerical Model, TermoFluids.

1. Introduction

Many authors have carried out experiments on several prototypes with innovative design concepts and studied the performance characteristics of LFR for different optical and geometric parameters (Barale et al., 2010 [1]; Beltagy et al., 2017 [2]; Bernhard et al., 2008 [3]; Häberle et al., 2001[4]; Negi et al., 1989 [5]; Singh et al., 1999 [6]). Linear Fresnel reflectors usually employ a secondary concentrator that enlarges the target área for primary mirrors, and also acts as protective cover to reduce convective losses. A number of authors have been studied different types of receivers such as trapezoidal cavity with multiple absorber tubes (Facão and Oliveira, 2011 [7]) triangular, rectangular, arc-shaped and semi-circular cavity receivers (Lin et al., 2014 [8]), modified V-shaped cavity. Qiu et al. (2015) [9] investigated the thermal performance of LFR that employs a compound parabolic concentrator (CPC) with an evacuated absorber. They concluded that uniformity of flux distribution can be improved by choosing a proper slope error, but with a small sacrifice in the optical efficiency.

The present work develops an advanced model of LFR, through a modular platform that works each part of the system as a unique element with the capacity to transfer information between one element and another, this union is realized by coupling heat flow and temperature, which provides numerical stability. This modular system allows to apply different models for the various heat transport mechanics (solids are treated with a 3D conducting solver, the fluid inside the cavity is treated with a CFD & HT coupled with a solver of thermal and solar radiation, the HTF you can apply a single/two phase model depending on an industrial oil, molten salt or water vapor).

A scheme of the Linear Fresnel Collector (LFC) is given in Fig 1. The cavity receiver of LFC consists of an absorber tube and a secondary concentrator. The Fresnel cavity profile is defined by an equation from the literature [13]. The absorber is usually protected with glass cover at the bottom of the cavity to reduce heat losses. The primary mirror field reflects the direct normal radiation into the cavity and due to astigmatism and optical inaccuracies only part of the reflected radiation hits the absorber directly. A fraction of the radiation interacts with the secondary reflector and is redirected onto the absorber. While the absorber is being heated, it

doi:10.18086/swc.2017.31.04 Available at http://proceedings.ises.org

loses heat by long wavelength radiation and convection to the surroundings.

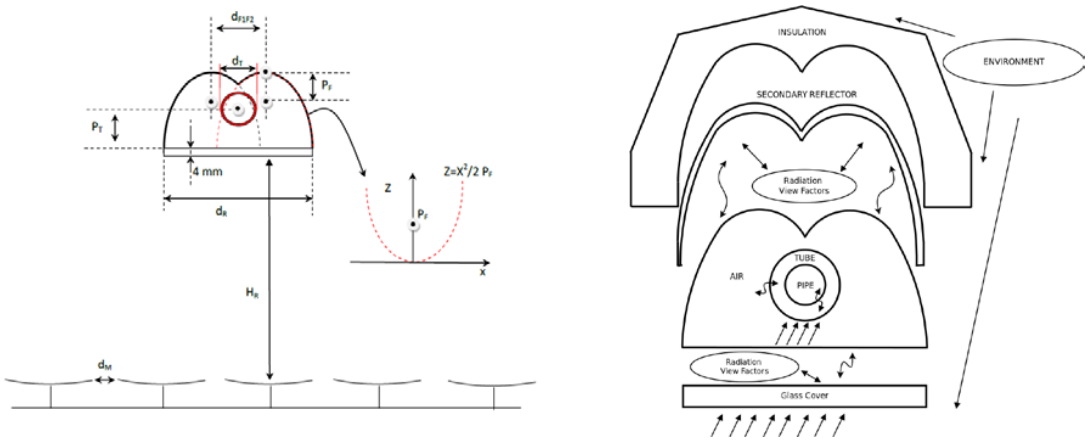

Fig. 1: NEST scheme of the modular system and Fresnel receiver

Nomenclature

c_p	Specific heat capacity, J kg^{-1} K^{-1}	Greek letters	
D_{in}	Internal diameter of the tube, m		
L_M	Width of mirror	ε	Thermal emissivity
f_M	Maximum deflection of the mirror	α	Sup. heat transfer coefficient, W m^{-2} K^{-1}
H_R	Receiver height	β	Thermal expansion coefficient, K^{-1}
d_R	Aperture of the receiver	η	Smallest turbulent scales of the flow, m
d_M	Distance between rows of mirrors	κ	Thermal diffusivity, m^2 s^{-1}
d_{F1F2}	distance between focal points	λ	Thermal conductivity, W m^{-1} K^{-1}
P_F	The focal parameter of the parabolic portions		
d_T	External tube diameter	μ	Dynamic viscosity, kg m^{-1} s^{-1}
P_T	Position of the tube in the cavity	ν	kinematic viscosity, m^2 s^{-1}
e_g	Thickness of the transparent glass	ξ	Turbulent kinetic energy dissipation rate, m^2 s^{-3}
η_{opt}	Optical efficincy	ρ	Density, kg m^{-3}
H	Height, m	σ	Stefan-Boltzmann constant, 5.67x10^{-8} W $m^{-2}K^{-4}$
g	Gravity vector, m s^{-2}	Γ_v	Stress tensor, m^{-2} s^{-2}
I	Identity matrix	Ω	volume, m^3
$\dot{m}$	Mass flow rate, kg s^{-1}	$\partial\mathbf{\Omega}$	Surface which enclosed the volume **Ω**, m^2
Nu	Nusselt number	Δ	Magnitude increment
n	normal direction vector		
Pr	Prandlt number, $Pr = \mu c_p/\lambda$	Subscripts	
Pr_t	Turbulent Prandlt number, $Pr_t=\nu_{sgs}/\kappa_{sgs}$		
$\dot{Q}$	Heat losses, W	conv	Convection
$\dot{q}$	Specific heat flux, W m^{-2}	rad	Radiation
Ra	Rayleigh number, $Ra = g\beta\Delta TH^3/\nu\kappa$	cond	Conduction
S	Surface area, m^2	ins	Insulation
S_{ij}	Rate-of-strain, m^2	gc	Glass cover
$\bar{S}_{ij}$	Mean rate-of-strain fluctuations, s^{-1}	amb	Ambient conditions
T	Temperature, K	ref	Reflectors
t	time, s	tube	Tube
z	extruded direction, m	in	Inlet conditions
f(t)	Function of the time	out	Outlet conditions
u	velocity vector, m s^{-1}	sgs	Subgrid scales
g_k	Irradiosity on surface *k*, W m^{-2}	dir	Direct Radiation
j_k	Radiosity on surface *k*, W m^{-2}	max	Maximum
<u>	Average velocity u, m s^{-1}		
DNI	Direct Normal Irradiance		

A modular object-oriented methodology for the design and optimization of Linear Fresnel receivers is proposed (NEST platform [10]). This methodology considers the different parts of the Linear Fresnel receiver as independent models and the coupling between global models and advanced computational fluid dynamic and

heat transfer (CFD&HT) mainly based on large-eddy simulation (LES) techniques (TermoFluids[11]).

TermoFluids [11], a general purpose unstructured and parallel object-oriented CFD code developed to solve industrial flows, is used to optimize the optical and thermal performance of a defined system (geometry, optical and thermal properties of the materials).

The presented methodology was explained by Guadamud et al (2014), [12]. For each element of the receiver more than one model approach is considered depending on the desired accuracy. The use of a modular simulation allows that for the same element one-, two- or three-dimensional models can be used. At the same time, each element can receive a special treatment from the physical point of view.

The implementation of the Fresnel receiver methodology has been made within the existing NEST platform which allows the linking between different elements to perform a specific system or configuration. In the present implementation, Fresnel receiver is considered as the sum of different parts, e.g. insulation, glass cover, air inside the cavity, tube, pipe, etc., such as shown in Fig 1.

2. Geometry configurations and optimization

Three different configurations were selected; table 1 shows all the parameters.

Table 1. Different configurations for the Linear Fresnel receivers

Parameters	Configuration 1	Configuration 2	Configuration 3
L_M	12.5% H_R	5% H_R	10.5% H_R
d_{F1F2}	8.5% d_R	0% d_R	0% d_R
p_F	10.2% d_R	15% d_R	12% d_R

The H_R represents the height of the receiver, for optical analysis, this value will vary to determine its effect on optical performance, in the thermal analysis will set this value constant for all three configurations to a value in which its optical behavior is the most optimum. The d_R (aperture of the receiver) will be fixed constant in both analysis, based on this, various aspect ratios are obtained as shown in Table 1.

The procedure of the optimization consists in fixing certain parameters (taking into account some technical criteria) and calculating the others parameters by maximizing the optical efficiency (considered as the objective function).

The variation of the DNI during the day is simulated by a cosine expression:

$$DNI(t) = DNI_{max} * \cos\left(\left(-\frac{\pi}{12}\right) * t + \pi\right) \quad \text{(eq. 1)}$$

For the optical efficiency (η_{opt}) is evaluated by the total energy received by the tube during the day between the direct normal irradiance with the reflectors surface, the second optical efficiency (η'_{opt}) is the total energy received by the tube during the day between the direct normal irradiance with the total surface of the land requirements.

3. Mathematical Model

3.1 Heat conduction in the solid elements of the Fresnel receiver (tube, glass cover and insulation).

Transient conduction heat transfer can be solved directly from the governing equation. For the case of the transient heat conduction without volumetric sources, the energy transport equation can be written in integral from as:

$$\rho c_p \frac{\partial T}{\partial t} = \nabla \cdot (\lambda \nabla T) \quad \text{(eq. 2)}$$

where T represents temperature, t is the time, ρ is density, c_p is the specific heat and λ the thermal conductivity. In this work, a non-structured mesh and a uniform distribution has been used in some elements like the tube and

the glass cover, but due to the geometric singularity in the element insulation the mesh has been adapted to this form.

In TermoFluids, for the integration of the governing equations the finite volume method has been used. A modified least-square method has been chosen for the calculation of the gradients. The resulting system of equations is solved by means of the Conjugate Gradient method [15].

3.2 CFD&HT of the air inside the cavity receiver

The objectives for using a CFD&HT object for modeling the air inside the cavity are twofold: (i) due to the complex geometry of the cavity, there are not specific correlations for the heat transfer inside irregular cavities, thus results of such modeling would be used for proposing new correlations to be used in the global model for the convective process and (ii) it would shed some light into the complex physics presents in this kind of receivers. The CFD&HT air cavity object calls TermoFluids CFD&HT code [11] which is an object-oriented parallel and unstructured CFD&HT code for the resolution of industrial flows. In this object, the three-dimensional Navier-Stokes equations are spatially filtered. Therefore, some level of modelisation for the filtered non-linear convective terms is required. This approach is known as large-eddy simulation (LES) of the turbulent flow. In LES, all temporal scales of the flow together with the largest spatial scales are solved, and only the small scales of the flow are modeled by means of a sub-grid scale model (SGS).

The discretised continuity, momentum and energy filtered equations, assuming constant thermophysical properties and negligible viscous dissipation effects in the energy equation read,

$$M\vec{u} = 0 \qquad \text{(eq. 3)}$$

$$\Omega\frac{\partial\vec{u}}{\partial t} + C(\bar{u})\bar{u} + vD\bar{u} + \rho^{-1}\Omega\bar{\mathrm{p}} - f = C(\bar{u})\bar{u} - \overline{C(u)u} \approx -M\Gamma \qquad \text{(eq. 4)}$$

$$\Omega\frac{\partial\overline{\mathrm{T}}}{\partial \mathrm{t}} + C(\bar{u})\bar{T} + \frac{\nu}{Pr}D\bar{T} - \overline{\nabla\cdot q_{rad}} = C(\bar{u})\bar{T} - \bar{C}(u)T \approx -M\Gamma_T \qquad \text{(eq. 5)}$$

where $\vec{u} \in R^{3m}$, $\bar{p} \in R^m$ and $\bar{T} \in R^m$are the filtered velocity vector, pressure and temperature, respectively (here m applies for the total number of control volumes (CVs) of the discretised domain). $\Omega \in R^{3m}$ is a matrix with the cell control volumes. f are the body forces, $f = \beta(T - T_{ref})\boldsymbol{g}$. Convective and diffusive operators are given by $C(\vec{\boldsymbol{u}}) = (\vec{\boldsymbol{u}}\cdot\nabla) \in R^{3m\times m}$, $D = -\nabla^2 \in R^{3m\times 3m}$ respectively. Gradient and divergence (of a vector) operators are given by $G = \nabla \in R^{3m\times m}$ and $M = \nabla\cdot R^{m\times 3m}$ respectively.

The last term in Eqs. (6) and (7) indicate some modelisation of the filtered non-linear convective term. M represents the divergence operator of a tensor, and Γ is the sub-gird scale (SGS) stress tensor, which is defined as[4],

$$\Gamma = -2v_{sgs}\overline{S_{ij}} + (\Gamma{:}\,\mathrm{I})I/3 \qquad \text{(eq. 6)}$$

where $\overline{S_{ij}} = 1/2[G(\vec{\boldsymbol{u}}) + G^*(\vec{\boldsymbol{u}})]$, and G^* is the transpose of the gradient operator. Γ_T term is evaluated as in Γ term, but v_{sgs} is substituted by v_{sgs}/Pr_t, where $Pr_t$is the turbulent Prandlt. To close the formulation, a suitable expression for the subgrid-scale (SGS) viscosity, v_{sgs}, must be introduced. The QR-model based on the invariants of the rate-of-strain tensor [15] has been used.

The governing equations used in TermoFluids CFD&HT code are discretised on a collocated unstructured grip arrangement by means of second-order conservative schemes [15], i.e. they preserve the kinetic energy equation which ensures stability and conservation of the kinetic-energy balance even at high Reynolds numbers and with coarse grids.

In the context of the large-eddy simulation of turbulent flows, the time advancement algorithm should be capable of solving all the relevant temporal scales while, at the same time, it should be kept within the stability domain. Different temporal schemes have been proposed in the literature to deal with time marching algorithm for turbulent flows (see for instance [16-18]). In this work, a two-step linear explicit scheme on a fractional-step method proposed by Trias and Lehmkuhl [19] is used. Its main advantage relies on its capacity of dynamically adapt the time step to the maximum possible value while at the same time it is kept within the stability limits. This strategy reduces the computational time required without lost accuracy. The method has been successfully

tested in different flows in [20-22].

3.3 Single phase flow

In this work, a one dimensional model has been chosen to represent the forced convection in the tube, solved by step by step method. The fact that this code is one dimensional makes difficult the communication between the fluid flow and the code for the tube heat conduction element. This problem has been solved by heat coupling between the tube and the pipe elements, evaluating the average heat flux of each n volume controls of the 3D tube element per plane of extrusion and passed to the pipe element, this average heat flux has been used to solve the fluid flow and a new temperature profile has been obtained, then this new temperature field has been used to evaluate the heat flow that has been send to the tube. A heat transfer coefficient has been calculated each time iteration considering the convective heat flux between the tube and the pipe in the extruded direction as:

$$\vec{q}_{tube-pipe,conv} = \sum_j \alpha_f \left(\bar{T}_{tube} - T_f^i\right) \frac{\pi D_{in}}{\Delta z} \qquad \text{(eq. 7)}$$

where α_f is the HTF convection heat coefficient at T_{tube} and is evaluated as a function of the Nusselt number Nu_{Din}, the Nusset number and the properties are evaluated at medium temperature between the temperature of the tube and the temperature of the fluid inside the tube. Due to the lack of specific correlations in literature for evacuation the Nusselt number taking into accont the temperature distribution of the tube, correlations for isothermal cylinders are considered. Specifically, the Gnielinski correlation [23] is used for turbulent and transitional flow (Re>3200) in circular ducts, which reads,

$$Nu_{D_{in}} = \frac{(C/2)\left(Re_{D_{in}} - 1000\right)Pr}{1+12\sqrt{C/8}\left(Pr^{2/3}-1\right)} \left(\frac{Pr}{Pr_w}\right)^{0.11} \qquad \text{(eq. 8)}$$

with $C = (1{,}82\log(Re_D)-1{,}64)^{-2}$.

A silicone HTF(Syltherm800)has been used, this fluid is normally used in CSP due to a highly stable at high temperature liquid phase operation. The thermo-physical properties of the syltherm 800 have been obtained from the datasheet [24], and the approaches have been made by a polynomial correlation, these properties correlation are presented in Table 2.

Table 2. Thermo-physical properties correlation of the Syltherm 800.

Property	Polynomial correlation
ρ	$1.269 \cdot 10^3 - 1.52\bar{T} + 1.8 \cdot 10^{-3}\bar{T}^2 - 2 \cdot 10^{-6}\bar{T}^3$
cp	$1.109 \cdot 10^3 + 1.7014\bar{T} + 1 \cdot 10^{-5}\bar{T}^2 - 9 \cdot 10^{-9}\bar{T}^3$
μ	$0.6527 - 6.451 \cdot 10^{-3}\bar{T}^3 + 2.552 \cdot 10^{-5}\bar{T}^2 - 5.023 \cdot 10^{-8}\bar{T}^3 + 4.905 \cdot 10^{-11}\bar{T}^4 - 1.9 \cdot 10^{-14}\bar{T}^5$
λ	$1.907 \cdot 10^{-1} - 2 \cdot 10^{-4}\bar{T} + 1 \cdot 10^{-8}\bar{T}^2 - 8 \cdot 10^{-12}\bar{T}^3$

3.4 Radiation

3.4.1 Solar Radiation from mirrors to receiver

The estimation of the incident solar energy was done by means of the Monte-Carlo Ray-tracing method, where a lightning sweep is performed on the various mirrors, the amount of energy incident on the tube is analyzed, and this amount of energy is saved for the different positions and is treated as a source term for the simulation of the system. The different matrixes obtained in the method will be loaded one by one each time it is considered suitable for which there has been a change of solar position and it is verified how it affects the Fresnel System.

a b

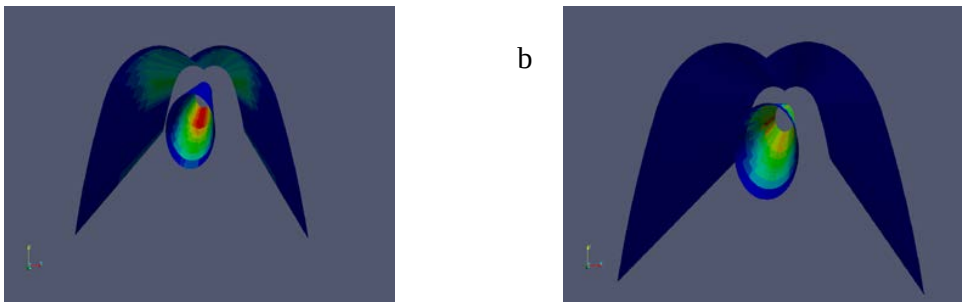

Fig. 2. Ray-tracing model obtained. (a) without a secondary reflector; (b) with a secondary reflector

Figure 2 shows the flux distribution of the incident solar radiation, comparing it qualitatively between a receiver without reflector (Fig. 2a) and with secondary reflector (Fig. 2b). In the first receiver the energy concentrates at lower part of the tube, losing many rays that go towards the upper part of the interior of the cavity, while having a secondary reflector distributes better the rays that do not directly affect the tube, and suffer second reflections increasing the optical performance of the system.

3.4.2 Thermal radiation inside the cavity

A Radiosity-Irradiosity method [25] has been applied to solve the non-participating media inside the cavity. The radiosity and the irradiosity can be expressed as:

$$j_k = \varepsilon_k E_{b,k} + \rho_k g_k \quad \text{(eq. 9)}$$

$$g_k = \sum_{l=1}^{N} F_{k\to l} j_l \quad \text{(eq. 10)}$$

For N surfaces, equations (11) and (12), define a linear system with N unknowns, the radiosities j_K. Once this system is solved, the toal heat flux, per unit area, is simply $q_K=j_K-g_K$. Considering the total heat flux $Q_K=A_K q_K$.

A Monte-Carlo Ray-tracing tool is applied to obtain the specular view factors needed, this factors are implemented on a Radiation model to solve a combined case with natural convection phenomena inside the cavity and their effects between the surfaces of the cavity and their surroundings.

4. Results

The need to analyze the behavior of a Fresnel Linear Receiver allows us to identify two important criteria, from the optical and thermal points of view.

The following is an intensive analysis of the various configurations, the parameters that determine its sensitivity, and has been compared with a commercial code such as OPSOL, obtaining very close results between those proposed by the RT-method of the CTTC and OPSOL [26]

Table 3. Optical efficiency comparison between this work and OPSOL code.

Parameters	Configuration 1	Configuration 2	Configuration 3
η_{opt}	*55%*	*57.5%*	*62.4%*
η'_{opt}	*39.5%*	*45.9%*	*48.4%*
η_{opt} **(OPSOL)**	*55%*	*60%*	*63%*
η'_{opt} **(OPSOL)**	*38.32%*	*46.8%*	*47.6%*

4.1 Optical performance of Linear Fresnel configuration

The instantaneous optical efficiency for the three configurations proposed was calculated for some day in April 2016 and based in Taroudant, Morocco. The analysis of the solar field behavior consisted on calculating the instantaneous power received by the tube during a whole day, from sunrise to sunset. The criteria to be optimized will be the effect of the receiver height, orientation of the mirrors, distribution of power in the symmetry plane, shadows basically.

4.1.1 Effect of receiver height.

It has been observed that increasing the height of the receiver results on a slightly higher performance. The reasons identified were: the orientation of the heliostats becomes more favorable, and the receiver being at a larger height casts less shadow on the mirrors.

4.1.2 Shadows

The shadows play a role in the efficiency of the system in two different ways. For the first and last hours of the day, when the sun altitude is low, some mirrors cast shadows onto other mirrors, thus decreasing the mirror surface area that reflects solar radiation to the receiver. On the other hand, when the sun is high in the sky, the receiver successively cast shadows one mirror by one mirror, thus also decreasing the effective area of the mirror. These two effects are illustrated in Figure 6.

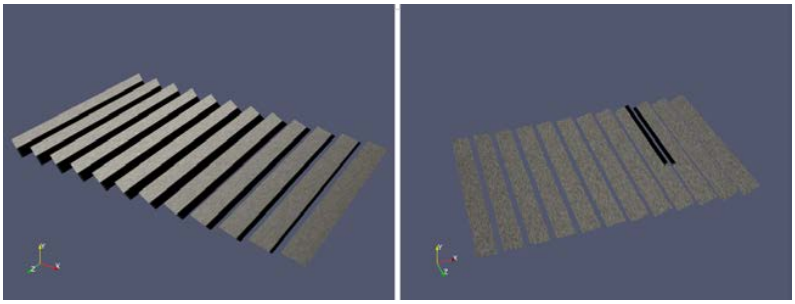

Fig. 6 Shadows cast on the mirrors are shown in black. Left: mirrors casting shadows on other mirrors when the sun is low in the sky. Right: receiver casting shadows on two mirrors when the sun is high in the sky.

It can be observed that the shadow casted by the receiver has less impact the higher the receiver is placed, because the shadow lasts for less time and covers less area of the mirrors. The fraction of the mirror that is illuminated during the course of the day, for several heights of the receiver, can be seen in Figure 7. The dents in the graphs correspond to the shadow of the receiver crossing the mirror, while the linear decrease at the end of the day (for outer mirror) and at both the beginning and end of the day (for the inner mirror) are due to the shadows cast by other mirrors. It is apparent from the figure that the effect of the shadows cast by the receiver is more detrimental for the configurations where the receiver is placed at lower a height. The effect of the shadows cast by other mirrors is (nearly) independent of the receiver height.

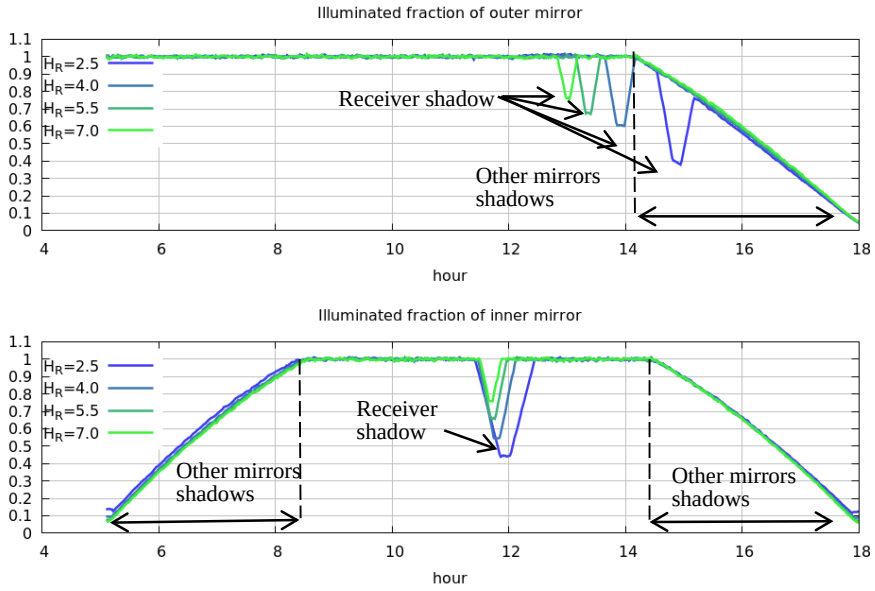

Fig. 7 Illuminated fraction of outer (top) and inner (bottom) mirrors, for several receiver heights.As the receiver height increases, both the size and duration of the shadow cast by the receiver decrease, making the mirror more effective.

4.1.3 Orientation of the mirrors

The orientation of the mirrors has an effect on the total power that can be reflected by the mirrors to the receiver and to the tube. Ideally, the mirrors should be facing a direction perpendicular to the direct solar radiation, but

there is a constraint that the orientation of the mirror is in fact determined by the point where it is supposed to focus the incoming solar radiation. Therefore, for a given receiver height and sun position, the orientation of the mirror is fixed. Looking at Fig. 3 one can expect that the orientation is more favorable the higher the receiver is placed, because the mirror will present a larger cross section to the solar radiation.

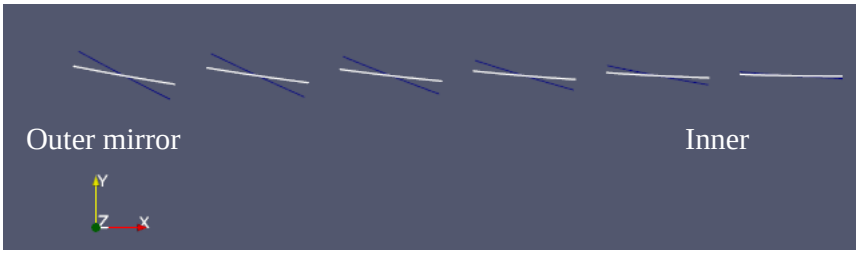

Fig. 3 Orientation of mirrors at noon. Blue mirrors: receiver height of 2m. White mirrors: receiver height of 8m. Taking into account that solar radiation at noon comes in Y direction (with some amount of Z component), clearly the higher the receiver height, the more effective area the mirrors present to the solar radiation. This effect is more important for the outer mirrors.

The influence of the orientation of the mirrors throughout the day is plotted in Figure 4. The inner mirror is the closest to the receiver, and the outer mirror is the furthest. The power reflected by the inner mirror due to its orientation is nearly independent of the receiver height. On the other hand, for the outer mirror the power reflected varies significantly with the receiver height.

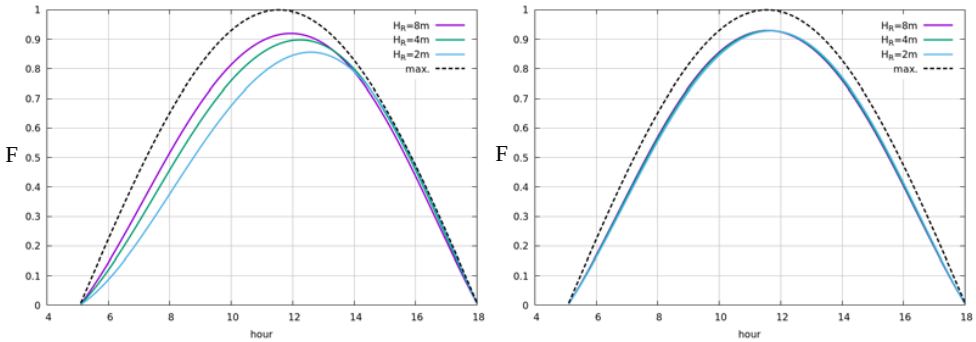

Fig. 4 Fraction of available solar power reflected by mirrors during the day. Geometric considerations only, i.e., the surface reflectivity of the mirror is not considered in these plots. Left: outer mirror (the higher the receiver, the more solar radiation is reflected). Right: inner mirror.

The daily integrated energy is shown in Figure 5. The closer the mirror is to the receiver (higher mirror index), the less influence the receiver height has on the power it can deliver. Note that the power reported is all of the power that is going to be reflected by the mirrors, without taking into account the distribution of this power in the zone near the receiver and the tube. In fact, not all of this power is going to be absorbed by the tube.

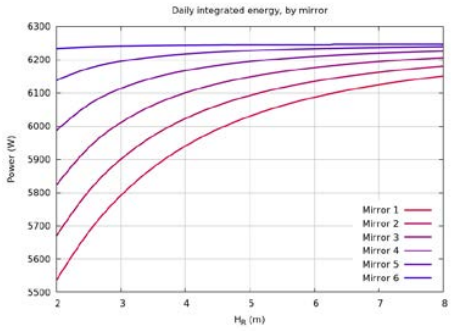

Fig. 5 Daily integrated energy for every mirror as a function of the receiver height. Inner mirror (6) is almost independent of H_R, while for outer mirrors (lower mirror index) the influence of H_R becomes noticeable.

4.1.4 Combination of all effects

To summarize, the receiver was collocated as high as possible so as to get less shadowing and higher cross section of the mirrors with respect to the incident solar radiation, but less power to the tube could available.

In Figure 8 the instantaneous power transferred to the tube is plotted for several heights of the receiver. It can be seen that the most optimal height roughly corresponds to that of the focal length of the parabolic mirrors. Also, the passage of the shadow of the receiver over the mirrors lasts less for higher heights (the wiggles start later and end before, and the time between two successive maxima is also shorter), and blocked area is smaller (the peak of variation is less pronounced).

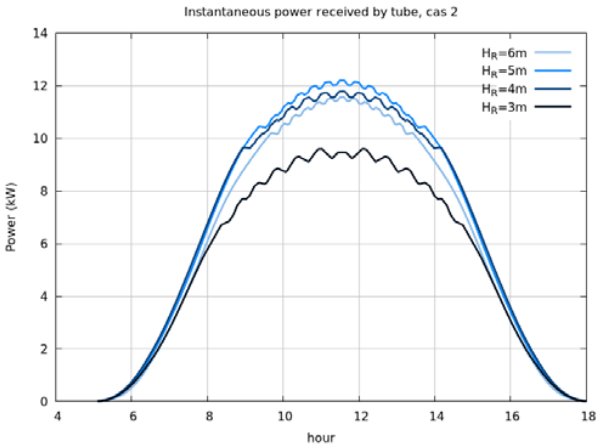

Fig. 8. Instantaneous power received by the tube in configuration "Cas 2" for several receiver heights.

4.2 CFD&HT modelling of the Fresnel receiver

4.2.1 CFD&HT modelling of the Fresnel receiver with radiation

The simulations were carried out with a direct intensity of variable radiation throughout the day. Similarities in the behavior and certain differences are presented in the different configurations. Due to the aspect ratio, visually there are differences, as shown in Figure 9. The first configuration has a double curve since there is a distance d_{F1F2} different from zero, whereas in the other two configurations only a single curve is presented. In the first configuration, the tube is situated at the vertical center of the cavity, in the second one is closer to the glass cover and in the third configuration; the tube is slightly higher than the vertical center of the cavity. At the energy level, the differences in position of the absorber tube, as well as the fact that there is a double parabola or only one, affect the temperature distribution. Higher values are observed in C1, than in the other two. Configurations 2 and 3 show similar temperatures.

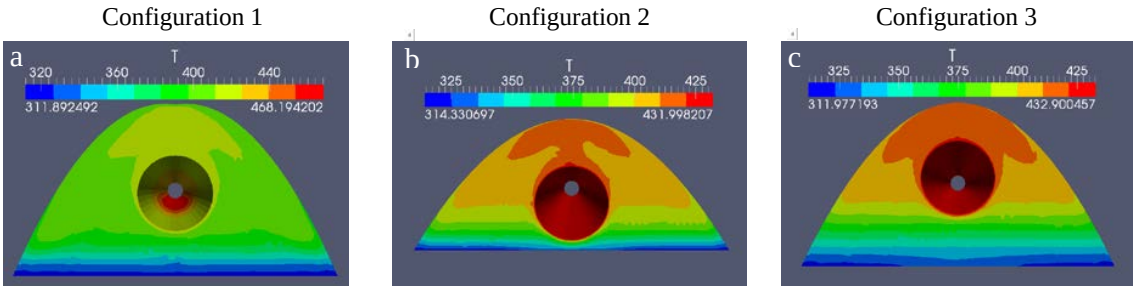

Fig. 9. Average air temperature (a) configuration 1; (b) configuration 2; (c) configuration 3

In the three configurations the tube with a higher temperature than its surroundings is observed, in configuration 3 there is a more closed concentration in the upper part of the cavity due to its closed curve, while in the two it is the more open, it is better distributed the temperature profile in this zone. In configuration 2, as the tube is closest to the glass cover, the Nusselt number is slightly higher, but the profile that reaches a higher peak is that of the first configuration. Figure 10 shows the distribution of the Nusselt number averaged in the air-tube absorber contact zone (Figure 10a) and in the air-insulation contact zone (Figure 10b). There is a change of trend in the Nusselt between the air and the insulation, because at the ends it is glued to the glass, where the air is at a lower temperature than that reached by the insulation, thus reversing the heat flow.

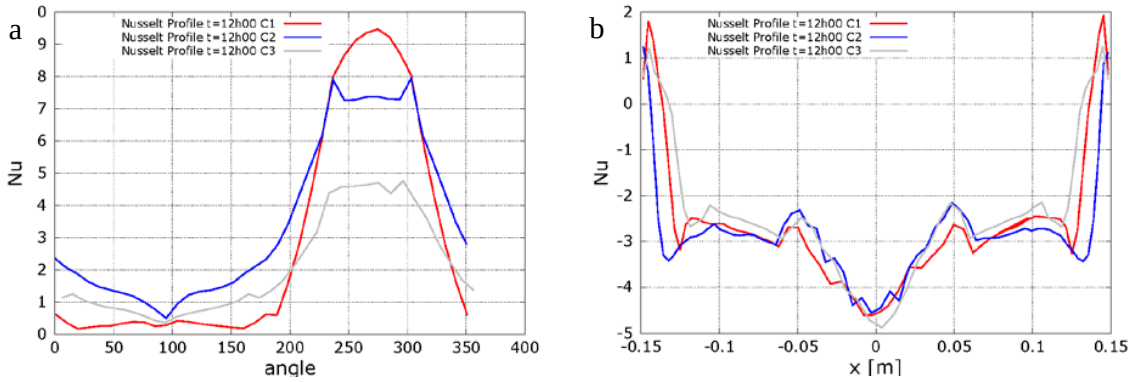

Fig. 10. Profiles of the average Nusselt number (a) boundary with tube; (b) boundary with insulation

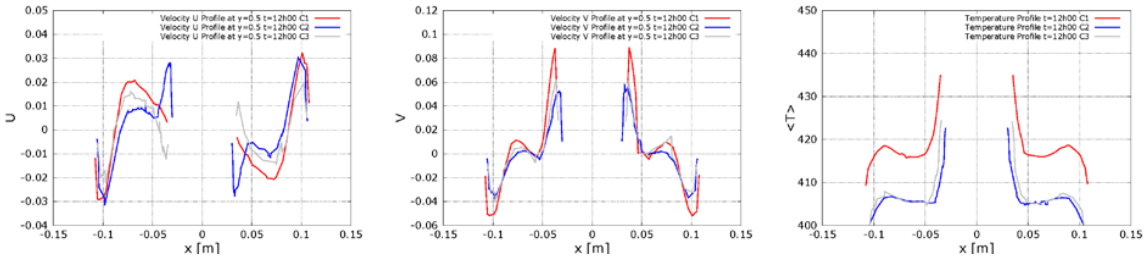

Fig. 11. Average profiles at middle of the cavity, plane z=1.0 (a) Velocity u profile from horizontal axis; (b) Velocity v profile from horizontal axis; (c) Temperature profile from horizontal axis.

Figure 11 shows the velocity profile for the various configurations at 12:00 solar time and ate the middle plane of the geometry (located at z = 1.0) in a horizontal line (parallel to the x-axis). In Figure 11a., it can be observed that the horizontal velocity u has a symmetrical but inverted behavior due to the geometry. In configuration 2, a more pronounced peak of horizontal velocity (u) is shown in the zone of contact with the tube. The accelerated decay of the value of u is due to the boundary layer conditions. The other two configurations show a lighter decay but with the same tendency. Figure 11b- shows the vertical velocity profile (v), where the symmetry of the case is visualized with respect to the center of the cavity. It is observed that, for this component of the velocity, the configuration with the highest peak is in the first. Moving away from the center, the downward tendency of the air is observed, reaching 0 at the contact end with the insulation. Figure 11c shows the temperature profile across the cavity from the zone of contact with the tube towards the insulation. It can be seen that the temperature is higher in the area close to the tube and decrease as it moves away towards the insulation. These values of temperatures could enhance the thermal wear of the system configurations 2 and 3 are more interesting.

4.2.2 Heat Conduction (Tube, Insulation and Glass Cover) and HTF inside the tube.

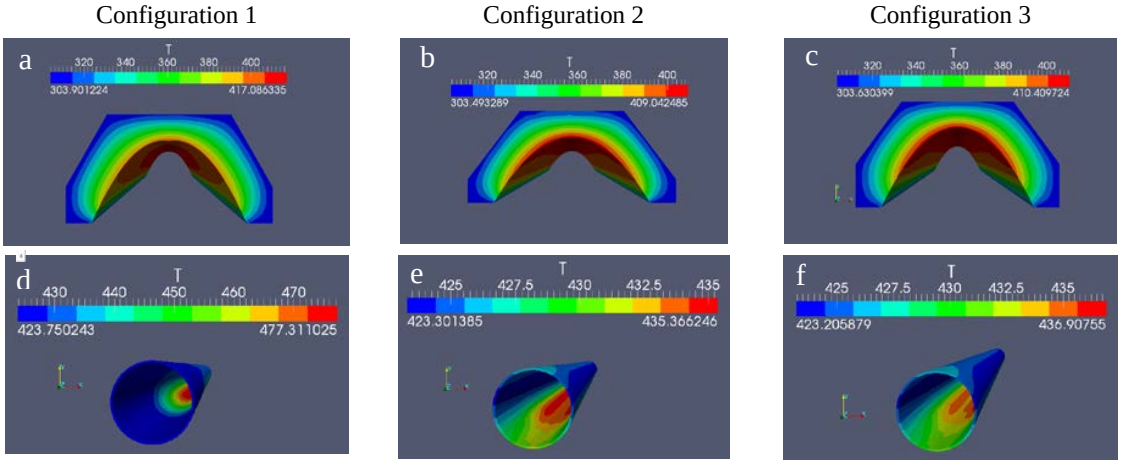

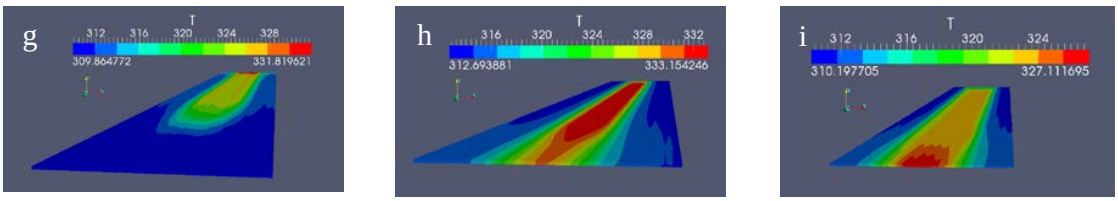

Fig. 12. Instantaneous distribution of the temperature, from top to bottom: insulation element, tube and glass cover. (a), (d), (g) configuration 1; (b), (e), (h) configuration 2; (c), (f), (i) configuration 3.

Figure 12 shows the instantaneous temperature profiles for each configuration and for each element of the system (insulation, absorber tube and glass cover). It is observed that the insulation has similar temperatures in the three configurations, even in the first case where a higher temperature is reached; it remains very similar, thermal expansion wear in this configuration must be taken into account. The absorber tube also has a high gradient between the inlet and the outlet, so it should be properly sized to withstand these temperatures and avoid thermal expansions that punish the element, configurations 2 and 3 exhibit similar behaviors with a variation of less than 2% of temperature in the tube and somewhat higher in the profile of the glass cover.

5. Conclusions

An advanced global model of a Fresnel linear system with couplings between natural convection, solar and thermal radiation, and its simultaneous multi-physics resolution allows us to estimate, study and analyze, the behavior of these systems in order to determine how is affected by the variation of the various parameters such as the height of the receiver, the shadows between mirrors, the orientation from the optical point of view. From the thermal point of view allows simulating diverse scenarios, to know maximum permissible temperatures. The coupled resolution also helps to determine the outlet temperature of the carrier heat fluid with a correct estimate, to test new materials, lighter or with lower optical properties, but to meet the energy requirements of these systems with the aim of reducing costs and making them more competitive with respect to other technologies of solar concentration.

The implementation of the system through a block where it can be varied of physical properties, the fluid carrier heat and the different models that are applied for its resolution, hypothesis, numerical approximations, etc., make this multidimensional model a versatile tool with many applications at industrial and energy sector level.

6. Acknowledgments

This research has been financed and supported by the European Institute of Technology and IRESEN through the Maghrenov project: “Solar Boiler based on Fresnel concentration system” (Ref. SIROCCO.EIT/KIC InnoEnergy/FPA/1).

7. References

[1] Barale, G., Heimsath, A., Nitz, P., Toro, A., 2010. Optical design of a Linear Fresnel collector for Sicily. In: SolarPaces Conf., pp. 1-7.

[2] Beltagy, H., Semmar, D., Lehaut, C., Said, N., 2017. Theoretical and experimental performance analysis of a Fresnel type solar concentrator. Renew. Energy 101, 782–793. http://dx.doi.org/10.1016/j.renene.2016.09.038.

[3] Bernhard, R., Laabs, H., De Lalaing, J., 2008. Linear Fresnel collector demonstration on the PSA, Part I–Design, construction and quality control. In: SolarPaces Conf., pp. 1–10. Breault Research Organization [WWW Document], n.d. (Accessed 04.10.17).

[4] Häberle, A., Zahler, C., De Lalaing, J., Ven, J., Sureda, M., Graf, W., Lerchenmüller, H., Wittwer, V., 2001. The solarmundo project - advanced technology for solar thermal power generation. In: ISES Sol. World Congr., pp. 961–970.

[5] Negi, B.S., Mathur, S.S., Kandpal, T.C., 1989. Optical and thermal performance evaluation of a linear Fresnel reflector solar concentrator. Sol. Wind Technol. 6, 589–593.

[6] Singh, P.L., Ganesan, S., Yàdav, G.C., 1999. Performance study of a linear Fresnel concentrating solar

device. Renew. Energy 18, 409–416. http://dx.doi.org/ 10.1016/S0960-1481(98)00805-2

[7] Facão, J., Oliveira, A.C., 2011. Numerical simulation of a trapezoidal cavity receiver for a linear Fresnel solar collector concentrator. Renew. Energy 36, 90–96. http://dx.doi.org/10.1016/j.renene.2010.06.003.

[8] Lin, M., Sumathy, K., Dai, Y.J., Zhao, X.K., 2014. Performance investigation on a linear Fresnel lens solar collector using cavity receiver. Sol. Energy 107, 50–62. http:// dx.doi.org/10.1016/j.solener.2014.05.026

[9] Qiu, Y., He, Y.-L., Cheng, Z.-D., Wang, K., 2015. Study on optical and thermal performance of a linear Fresnel solar reflector using molten salt as HTF with MCRT and FVM methods. Appl. Energy 146, 162–173. http://dx.doi.org/ 10.1016/j.apenergy.2015.01.135

[10] Damle, R., Lehmkuhl, O., Colomer, G., Rodríguez, I., 2011. Energy simulation of buildings with modular object oriented tool. In: ISES World conference; P. 1-8.

[11] Lehmkuhl, O., Pérez Segarra, C. D., Borrel, R., Soria, M. And Oliva, O., 2007, TermoFluids: A new Parallel unstructured CFD code for the simulation for turbulent industrial on low cost PC CLUSTER. Proceddings of Parallel CFD 2007 Conference, pq. 1-8.

[12] Guadamud, E. Oliva, A., Lehmkuhl, O., Rodríguez, I. And González, I. 2014. Thermal analysis of a receiver for Linear Fresnel reflectors. SolarPaces2014: International Conference on Concentrating Solar Power and Chemical Energy Systems: proceedings, at “Energy Procedia”, vol. 69, Pags: 405-414. ISBN/ISSN: 1876-6102, May 2015.

[13] Dixon, J. D., Davies, P. A., 2012 Cost-exergy optimisation of linear Fresnel reflectors. Solar Energy, Vol. 86, pp 147-156.

[14] Sagaut P, Germnao M: Large eddy simulation for incompressible flows. Sporinger-Verlag; 2001.

[15] Verstappen RWCP, Veldman AEP. Symmetry-preserving discretization of turbulent flow. Jornal Of Computational Physics, 187:343-368, May 2003.

[16] Le H, Moin P. An improbvement of fractional step methods for incompressible Navier-Stokes equations. Journal of Computational Physics 1991;92(2):369-79.

[17] Kim D, Choi H. A second order time-accurate finite volume method for unsteady incompressible flow on hybryd unstructured grids. Journal of Computational Physics 2000;162(2):411-28.

[18] Fishpool G, Leschziner M. Stability bounds for explicit fractinal-step schemes for Navier-Stokes equations at high Reynolds number. Computers & Fluids 2009;38:1289-98.

[19] Trias F, Lehmkuhl O, A self-adaptive strategy for time integration of Navier-Stokes equations. Numerical Heat transfer Part B 2011;60(2):116-34.

[20] Trias F, Gorobets A, Soria M, Oliva A. Direct numerical simulation of a differentially heated cavity of aspect ratio 4 with rayleigh numbers up to 1011. Part i: numerical methods and time-averaged flow. International Journal of Heat and Mass Transfer 2010;53(4):665-73.

[21] Rodríguez I, Lehmkuhl O, Borrell R, Oliva A. Flow dynamics in the wake of a sphere at sub-critical Reynolds numbers. Computers & Fluids 2012.

[22] Jaramillo J, Trias F, Gorobets A, Pérez-Segarra C, Oliva A. DNS and RANS modelling of a turbulent plane impinging jet. International Journal of Heat and Mass Transfer 2012;55(4):789-801.

[23] Gnielinski V. New equations for heat and mass transfer for turbulent pipe and channels flow. Int Chem Eng 1976:16(2):359-63.

[24] Syltherm 800, Heat Transfer Fluid. Availabled in: www.loikitsdistribution.com/files/syltherm-800-product-brochuere.pdf

[25] Michael F. Modest. Radiative Heat Transfer. McGraw Hill, 1993.

[26] Soukaina El Alj, Ahmed Almers, et al. “Optical Modelling and Analysis of the First Moroccan Linear Fresnel Solar Collecto Prototype”, Journal of Solar Energy Engineering, Transactions of ASME; 139[5], 0410091-12, 2017.